A sub-Neptune transiting the young field star HD 18599 at 40 pc

J. P. de Leon [1]★ J. H. Livingston [1,2,3,4] J. S. Jenkins [5] J. I. Vines [6] R. A. Wittenmyer [7]
J. T. Clark [7] J. I. M. Winn [8] B. Addison [7] S. Ballard [9] D. Bayliss [10] C. Beichman [11]
B. Benneke [12] D. A. Berardo [13] B.P. Bowler[14] T. Brown[15,16] E. M. Bryant [17] J. Christiansen [11]
D. Ciardi [11] K. A. Collins [18] K. I. Collins [19] I. Crossfield [20] D. Deming [21,22] D. Dragomir [23]
C. D. Dressing [24] A. Fukui [25,26] T. Gan [27] S. Giacalone [24] S. Gill [10,28] V. Gorjian [29]
E. González Alvarez[30] K. Hesse [31] J. Horner [7] S. B. Howell [32] J. M. Jenkins[33] S. R. Kane [34]
A. Kendall[35] J. F. Kielkopf [36] L. Kreidberg [18] D. W. Latham [18] H. Liu[37] M. B. Lund [11]
R. Matson [32] E. Matthews [13,38] M. W. Mengel [7] F. Morales [29] M. Mori [1] N. Narita [2,25,39]
T. Nishiumi [2,4,40] J. Okumura[7] P. Plavchan [19] S. Quinn [18] M. Rabus [41,42,43] G. Ricker [13]
A. Rudat,[13] J. Schlieder [44] R. P. Schwarz [18] S. Seager [13,45,46] A. Shporer [13] A. M. S. Smith,[47]
K. Stassun [48,49] M. Tamura [1,2,3] T. G. Tan [50] C. Tinney [51] R. Vanderspek [13] M. W. Werner,[29]
R. G. West,[10,28] D. Wright [7] H. Zhang[52] and G. Zhou [7,18]

Affiliations are listed at the end of the paper

ABSTRACT

Transiting exoplanets orbiting young nearby stars are ideal laboratories for testing theories of planet formation and evolution. However, to date only a handful of stars with age <1 Gyr have been found to host transiting exoplanets. Here we present the discovery and validation of a sub-Neptune around HD 18599, a young (300 Myr), nearby ($d = 40$ pc) K star. We validate the transiting planet candidate as a bona fide planet using data from the *TESS*, *Spitzer*, and *Gaia* missions, ground-based photometry from *IRSF*, *LCO*, *PEST*, and *NGTS*, speckle imaging from Gemini, and spectroscopy from *CHIRON*, *NRES*, *FEROS*, and MINERVA-Australis. The planet has an orbital period of 4.13 d, and a radius of 2.7 $R_\oplus$. The RV data yields a 3-σ mass upper limit of 30.5 $M_\oplus$ which is explained by either a massive companion or the large observed jitter typical for a young star. The brightness of the host star ($V{\sim}9$ mag) makes it conducive to detailed characterization via Doppler mass measurement which will provide a rare view into the interior structure of young planets.

Key words: techniques: radial velocities – techniques: spectroscopic – planets and satellites: detection – stars: individual: TOI-179.

1 INTRODUCTION

The majority of currently known exoplanets orbit mature host stars. In order to have a complete understanding of how planetary systems evolve from birth to maturity, we need to have a sample of systems at various evolutionary stages. In particular, young exoplanets (<1 Gyr in age) inhabit a very important part of the exoplanet evolutionary time-scale, where formation mechanisms, accretion, migration, and dynamical interactions can significantly change the shape of observed planetary systems.

This is well illustrated by our knowledge of the planetary system for which we have by far the most information – the Solar system. When we study the Solar system's history, it is immediately apparent that the first few hundred million years were an extremely chaotic and volatile time, with the system evolving dramatically on short time-scales. Evidence abounds of the giant impacts that shaped both the terrestrial and giant planets, including the big smash which led to Mercury's reduced size and enhanced density (e.g. Benz, Slattery & Cameron 1988; Benz et al. 2007; Chau et al. 2018), the collision that shattered the proto-Earth and formed the Moon (e.g. Benz, Cameron & Melosh 1989; Canup & Asphaug 2001; Canup 2012), the potential origin of Mars' hemispheric anomaly (e.g. Andrews-Hanna, Zuber & Banerdt 2008), the formation of Jupiter's diluted core (e.g. Liu et al. 2019), and Uranus' peculiar axial tilt (e.g. Slattery, Benz & Cameron 1992; Parisi & Brunini 1997; Kegerreis et al. 2018). At the same time, the system's small body populations reveal the scale of the migration of the giant planets. In the case of Uranus and Neptune, those small bodies reveal a significant outward migration.[1] (e.g. Lykawka et al. 2010, 2011). In the case of Jupiter and Saturn, the evidence points to significant inward migration, and potentially

---

★ E-mail: jpdeleon@g.ecc.u-tokyo.ac.jp

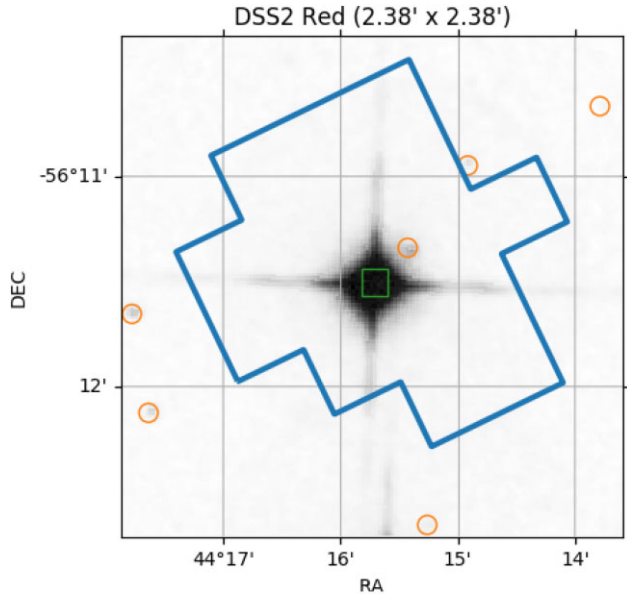[1] in the case of Neptune, travelling over at least 10 AU

Figure 1. 3 arcmin × 3 arcmin DSS2 (blue filter) image showing the target (green square) on the centre and nearby *Gaia* sources (orange circles), superposed with the Sector 2 SPOC photometric aperture (blue polygon). We establish a dilution of <1 per cent for HD 18599 based on the flux contributions of all sources within or near the aperture perimeter.

Table 1. HD 18599 photometric data.

Time [BJD-2450000)]	Flux	σ	Instrument
8354.1116	1.0007	0.0004	*TESS*
8354.1130	1.0009	0.0004	*TESS*
8354.1157	1.0012	0.0004	*TESS*
⋮	⋮	⋮	⋮

Note. This table is published in its entirety in a machine-readable format. A few entries are shown for guidance regarding form and content.

(CKS) sample increases with system age between 1 and 10 Gyr even without accounting for completeness effect. Relative to sub-Neptunes, super-Earths appear to be more common around older stars despite the difficulty of detecting small planets around larger stars. Moreover, David et al. (2020) found that the size distribution of small planets also depends on the age of the planet population and that the precise location of the radius valley changes over gigayear time-scales. However, we are still in the early stages to confidently corroborate or refute such trends given the low number of transiting planets orbiting young stars. Therefore, by compiling a statistically significant sample of well-characterized exoplanets with precisely measured ages, we should be able to begin identifying new trends as well as other dominant processes governing the time-evolution of exoplanet systems.

Here we present the discovery and validation of a sub-Neptune around HD 18599 also known as TOI 179, a young (300 Myr), nearby ($d = 38.6$ pc) K star. In Section 2, we discuss the observations including the discovery data from *TESS*, follow-up photometry from space by *Spitzer* and from the ground by several telescopes, archival photometry, and kinematics from *Gaia*, spectroscopy from MINERVA-Australis, *FEROS*, *CHIRON*, and *NRES*, and speckle imaging from Gemini. In Section 3, we present our analyses to characterize the host star and in particular establish its youth. In Section 4, we derive the properties of the planet such as its precise radius and mass limit. We also synthesize all available data to validate the planet candidate. In Section 5, we put the planet in context with the known young population. Finally, we summarize our results in Section 6 and also motivate further follow-up efforts of HD 18599 to measure the planet's mass and potentially characterize its interior and atmosphere.

a period of significant dynamical instability although the scale, rate, and chaoticity of that migration remains the subject of much debate (e.g. the Nice model: Tsiganis et al. (2005), the Grand Tack: O'Brien et al. (2014) and Walsh et al. (2012); or a smoother, less chaotic migration: Lykawka & Horner (2010) and Pirani et al. (2019). For a detailed overview of our knowledge of the Solar system, tailored towards Exoplanetary Science, we direct the interested reader to Horner et al. (2020).

To date, only a handful of exoplanet host stars have a well-constrained age. The youngest known transiting systems so far include K2-33 (age = 5–10 Myr; David et al. 2016; Mann et al. 2016), TOI-1227 (9–13 Myr; Mann et al. 2022), HIP 67 522 (15–19 Myr; Rizzuto et al. 2020), Au Mic (19–25 Myr; Plavchan et al. 2020), TOI 1097 (24–30 Myr; Wood et al. 2022), V1298 Tau (24–32 Myr; David et al. 2019; Johnson et al. 2022), KOI-7368 & KOI-7913 (28–46 Myr; Bouma et al. 2022a), TOI 837 (30–46 Myr; Bouma et al. 2020), Kepler-1627A (32–44 Myr; Bouma et al. 2022b), DS Tuc A (40–50 Myr; Newton et al. 2019), Kepler-1643 (39–55 Myr; Bouma et al. 2022a), and Kepler-970 & Kepler-1928 (95–115 Myr; Barber et al. 2022). The rarity of known young planets is attributed to the difficulties involved in their detection – the large intrinsic stellar activity in young stars that induces large photometric variations and radial velocity (RV) jitter often a few orders of magnitude larger than the planet signal (e.g. Heitzmann et al. 2021; Nicholson et al. 2021). Recently, novel methods have been developed to overcome this problem by using a method to detrend both photometry and RV data (e.g. Dai et al. 2017; Collier Cameron et al. 2021). Despite the small sample of planets detected so far, there is tentative evidence that there is a measurable change in the occurrence rates of planets with time (see Fig. 14; Mann et al. 2016), although more samples are needed to robustly confirm this trend. More recently, Berger et al. (2020) and Sandoval, Contardo & David (2020) found that the ratio of super-Earth to sub-Neptune detections in the California-Kepler Survey

2 OBSERVATIONS

2.1 Photometry

We summarized below all the photometric observations we conducted and used in our analyses, including the initial *TESS* discovery, follow-up observations with *Spitzer* and several ground-based telescopes, and archival data. The measurements are given in Table 1.

2.1.1 TESS *discovery*

HD 18599 was observed by *TESS* in sectors 2 (2018 August 22–September 2 UT) and 3 (2018 September 20–October 18 UT) during its first year with 2-min cadence as shown in Fig. 1, and sectors 29 (2020 August 26–September 22 UT) and 30 (2020 September 22–October 21) during its third year with 20-s cadence as shown in see Fig. 2. The photometric data were processed by the Science Processing Operations Center (SPOC; Jenkins et al. 2016) data reduction pipeline which produced time-series light curves for each campaign using Simple Aperture Photometry (SAP), and the Pre-search Data Conditioning (PDCSAP) algorithm (Smith et al. 2012;
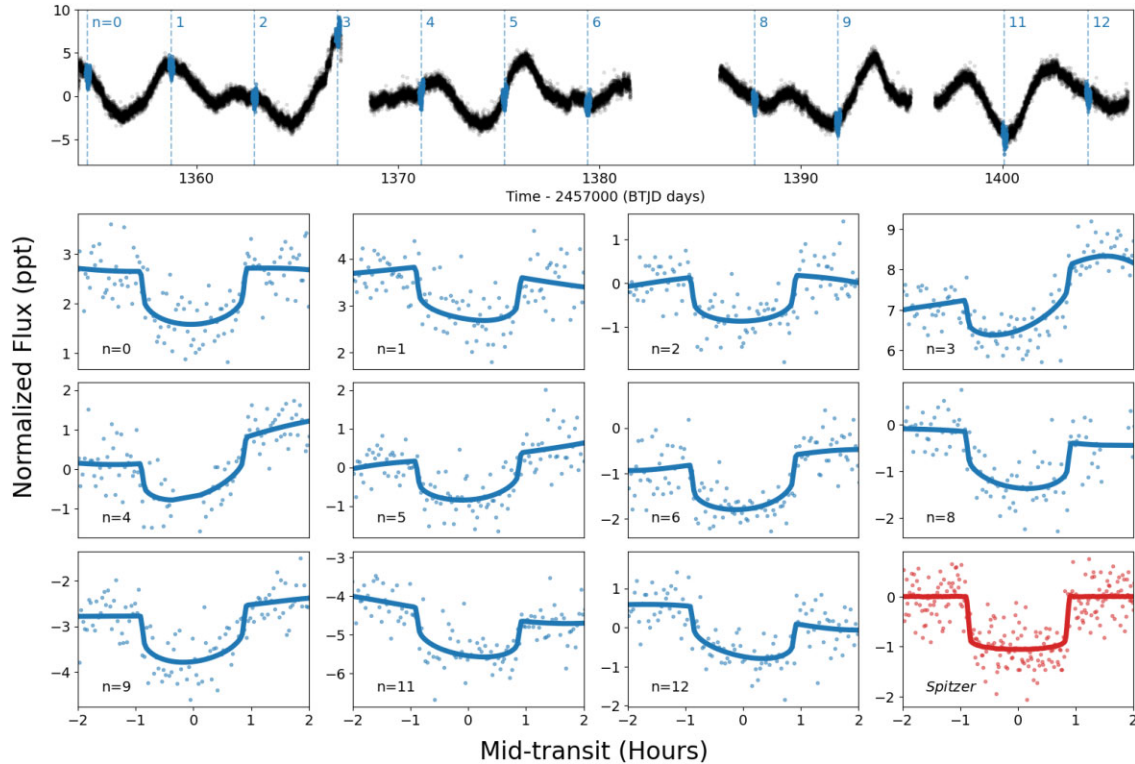
Figure 2. Raw light curves used in transit modelling superposed with best-fitting transit model with baseline trend. The top row shows the *TESS* PDCSAP light curves (cadence = 2 min) in sectors 2 & 3 where the individual transits are highlighted in blue and numbered relative to the first ($n = 0$). Panels 2 to 12 show the zoomed-in view of individual transits with best-fitting models. The last panel shows the *Spitzer* light curve.

Stumpe et al. 2012). For our analysis, we used the PDCSAP light curves which have been corrected for the instrumental and systematic errors as well as light dilution effects from nearby stars. The time-series in each sector has a ~4-d gap because of the data downlink and telescope re-pointing.

The *TESS* object of interest (TOI) releases portal[2] announced the transiting planet candidate around HD 18599 (TIC 207141131) as TOI 179 .01 (Guerrero et al. 2021). The candidate passed all tests from the Alerts Data Validation Report (Twicken et al. 2018) and is listed on the Exoplanet Follow-up Observing Programme (ExoFOP)[3] web page as having a period of 4.1374 d and a transit depth of about 1097 ppm .

2.1.2 Spitzer *follow-up*

We obtained observations of HD 18599 with the intention of following up the candidate planet using the Infrared Array Camera (IRAC; Fazio et al. 1998) 4.5 μm channel, as part of *Spitzer* TESSTOO program 14 084 (P.I. Crossfield). Observations with *Spitzer* have a number of advantages over those taken by *TESS*. First, *Spitzer* has a smaller pixel scale (1.2 arcsec pix^{-1}) than that of *TESS*'s (21 arcsec pix^{-1}). This allows *Spitzer* observation to localize the signal by excluding the nearby stars that are blended with the target star in the *TESS* photometric aperture (see Fig. 1). Secondly, the effects of limb darkening in *Spitzer* is reduced because it operates in the near-infrared, relative to *TESS* which operates in the optical. Thirdly, *Spitzer* has better sampling of the transit due to the shorter

(2-s) cadence of our *Spitzer* data compared to the shortest available *TESS* (20-s) cadence. Hence, more accurate planet parameter estimates are obtained when modelling the *Spitzer* transit light curve jointly with *TESS*. In conjunction with the *TESS* bandpass, the 4.5 μm IRAC bandpass also provides a relatively broad wavelength baseline which is very useful for planet validation (See Section 4.4).

We used integration time of 2 s to keep the detector from saturating and minimize data downlink bandwidth. Following Ingalls et al. (2016), the target was placed on the 'sweet spot' of the detector ideal for precise time-series photometry of bright stars like HD 18599 . We then extracted the *Spitzer* light curves following Livingston et al. (2019) which was based on the approach taken by Knutson et al. (2012) and Beichman et al. (2016). In brief, we compute aperture photometry using circular apertures centred on HD 18599 , for a range of radii between 2.0 and 5.0 pixels, corresponding to 2.4 arcsec–6.0 arcsec. We used a step size of 0.1 pixel from 2.0 to 3.0, and a step size of 0.5 from 3.0 and 5.0. The optimal aperture was selected by minimizing the photon noise due to sky background and correlated noise due to inter- and intrapixel gain variations. The resulting light curve is shown in the last panel of Fig. 2.

2.1.3 IRSF *follow-up*

We also conducted ground-based follow-up transit observation of HD 18599 on 2018 October 16 using the SIRIUS camera (Nagayama et al. 2003) on-board the 1.4-m Infrared Survey Facility (IRSF) telescope located in Sutherland, South Africa. The instrument is capable of simultaneous imaging in *J*, *H*, K_s bands which is ideal
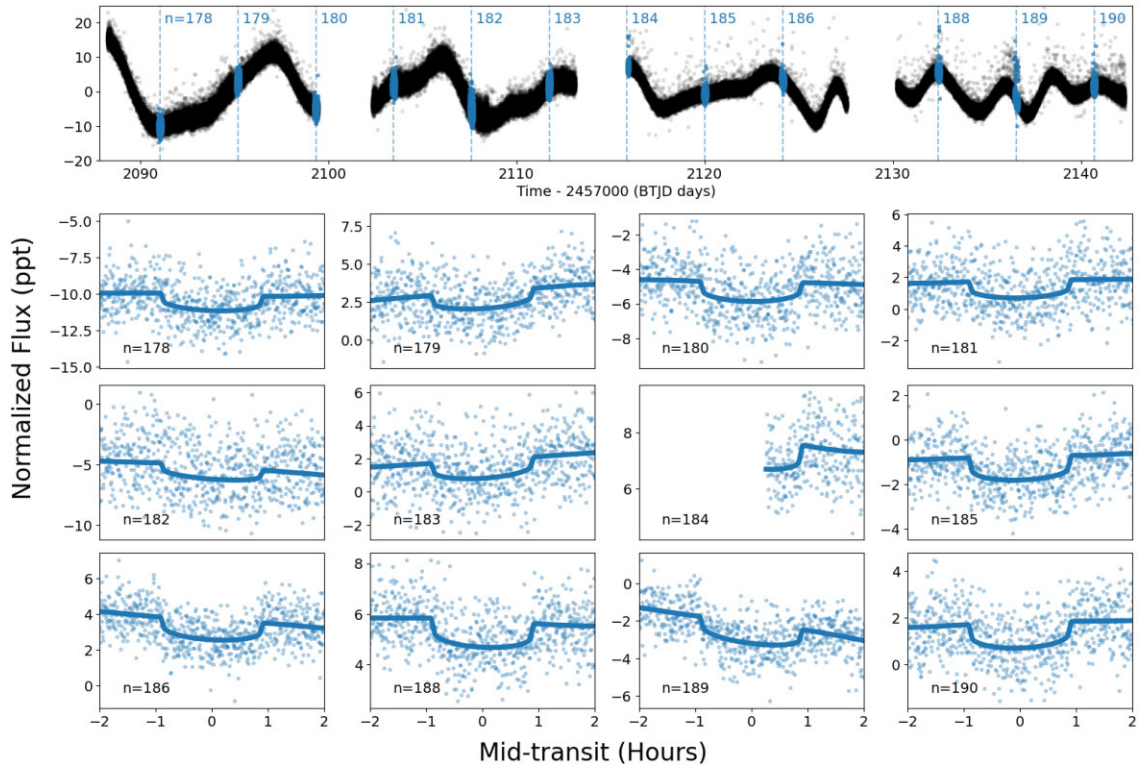
Figure 3. Same as Fig. 2 but for *TESS* sectors 29 and 30. Note the significantly higher sampling rate due to the shorter (20-s) cadence.
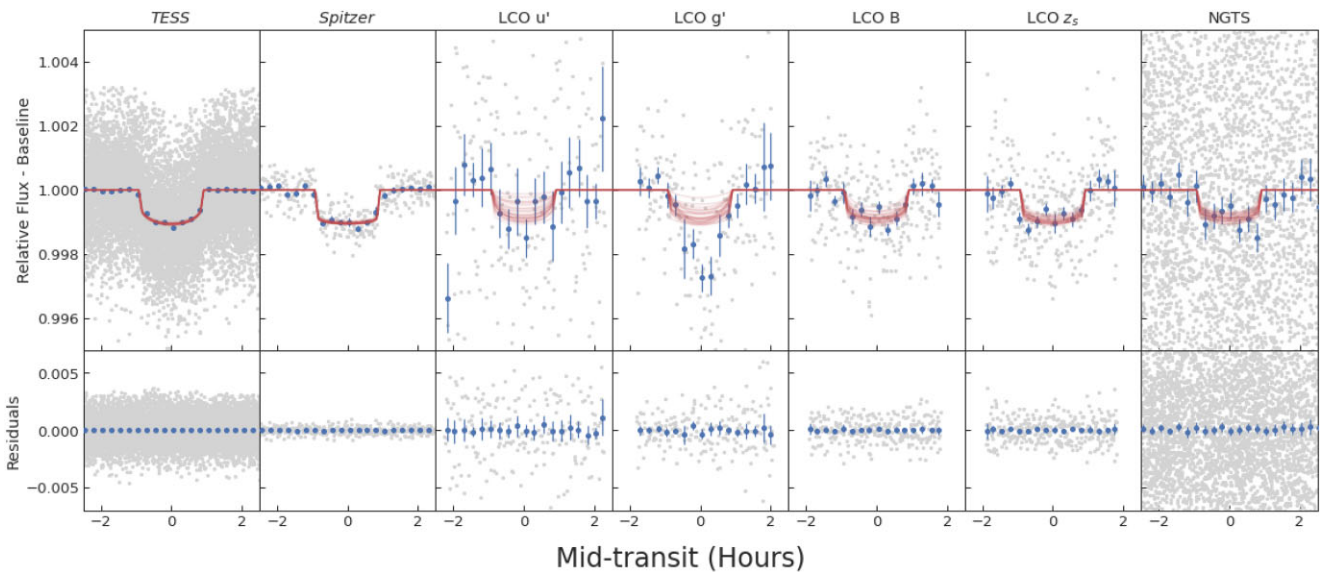

Figure 4. Light curves used in this work. The top row shows the phase-folded data with best-fitting transit models (see Section 4.2). The blue data points show binned data every 2-min and red lines show a fit using random samples from the MCMC posterior. The bottom row shows the residuals between the data and the transit + systematics model.

for planet validation. We created light curves in three bands using the standard reduction method and aperture photometry following Narita et al. (2013). Although we were not able to detect the shallow 1.1 ppt (parts per thousand) event on target in all bands, we were able to rule out the deep eclipses from nearby faint stars that could reproduce the *TESS* detection. This adds further evidence that the signal indeed originates from HD 18599 as shown in Section 2.1.2.

2.1.4 LCO *follow-up*

We observed HD 18599 on 2021 September 18 with 1.0 m *LCO* - CTIO in the *B* and z_s bands, on 2018 November 18 with 1.0 m *LCO* - CPT in the g' band, on 2018 November 23 with the 1.0 m *LCO* -CTIO in the u' band, and on 2018 December 22 with the 0.4 m *LCO* -CTIO in the i' band. All observations were full transit except that one taken in the i' band. We scheduled our transit observations using the

`TESS Transit Finder`, which is a customized version of the TAPIR software package (Jensen 2013). The photometric data were calibrated and extracted using `AstroImageJ` (Collins et al. 2017). Comparison stars of similar brightness were used to produce the final light curves, each of which showed a roughly 2-ppt dip near the expected transit time. The observations are summarized in Table 2 and plotted in Fig. 3.

2.1.5 NGTS *follow-up*

We observed HD 18599 on 2019 November 21 using *NGTS* (Next Generation Transit Survey) based at ESO's Paranal Observatory in Chile. This array of twelve 0.2 m telescopes is equipped with 2K×2K e2V deep-depleted Andor Ikon-L CCD cameras with 13.5 μm pixels, corresponding to an on-sky size of 4.97 arcsec, each with a custom *NGTS* (550–927 nm) filter. These observations were performed in the 'multi-telescope' observing mode (Smith et al. 2020), using three of the *NGTS* telescopes simultaneously. The data were reduced using a custom aperture photometry pipeline (Bryant et al. 2020), which uses the SEP library for both source extraction and photometry (Bertin, E. & Arnouts, S. 1996; Barbary 2016).

2.1.6 PEST *followup*

We observed HD 18599 in the I_C band from the Perth Exoplanet Survey Telescope (PEST) near Perth, Australia. The 0.3 m telescope is equipped with a 1530 × 1020 SBIG ST-8XME camera with an image scale of 1.2 arcmin pixel^{-1} resulting in a 31 arcmin × 21 arcmin field of view. A custom pipeline based on `C-Munipack`[4] was used to calibrate the images and extract the differential photometry.

2.1.7 KELT *archival data*

HD 18599 was observed as part of the Kilodegree Extremely Little Telescope (KELT) survey using a 42 mm-aperture telescope located in Sutherland, South Africa (Pepper et al. 2012). The telescope is equipped with Mamiya 645 80 mm f/1.9 42 mm lens with a 4k×4k Apogee CCD, a pixel scale of 23 arcsec and a field of view of 26° × 26°. The target was observed with a 20–30 min cadence. The data were reduced in a standard manner using the pipeline described in detail in Siverd et al. (2012) and Kuhn et al. (2016).

2.2 Spectroscopy

We conducted several high resolution spectroscopic observations to characterize the host star and to measure the RV variation induced by an orbiting companion. In the following, we describe our observations first and then derive an upper mass limit of the companion. The measurements are given in Table 3, and shown in Fig. 4.

2.2.1 FEROS

We obtained nine spectra with typical exposure time of 600 s conducted between 2019 September 10 and 19 UT using *FEROS* echelle spectrograph with a resolution $R = 48\,000$, wavelength coverage between 350 and 920 nm, and mounted on the MPG/ESO-2.2 m telescope in La Silla, Chile (Kaufer et al. 1999). The spectra have a

typical SNR of 80. The observations were performed in the Object-Calibration mode to allow precise RV observations. The spectra were then processed with the CERES pipeline (Brahm, Jordán & Espinoza 2017) to obtain both RVs and activity indicators.

2.2.2 MINERVA-*Australis*

The MINiature Exoplanet Radial Velocity Array (MINERVA)-Australis is an observatory located in Queensland, Australia, dedicated to the precise radial-velocity and photometric follow-up of *TESS* planet candidates (e.g. Addison et al. 2019, 2021; Wittenmyer et al. 2022). It consists of four 0.7 m robotic telescopes fibre-fed to a KiwiSpec spectrograph with spectral resolution of ∼80 000 and wavelength coverage between 480 and 620 nm (Wilson et al. 2019).

We obtained 31 spectra of HD 18599 between 2019 January 6 and 29 with a typical exposure time of 20–30 min. Radial velocities for the observations are derived for each telescope by cross-correlation, where the template being matched is the mean spectrum of each telescope. The instrumental variations are corrected by using simultaneous Thorium-Argon arc lamp observations.

2.2.3 CTIO/CHIRON

We conducted high resolution spectroscopy of HD 18599 using CTIO High Resolution spectrometer (*CHIRON*) on the 1.5-m SMARTS telescope. It has a spectral resolution of 80 000 with wavelength coverage between 4500 and 8900 Å. Between 2019 February and 2020 December, we took a total of 6 spectra with typical SNR between 53 and 130.

2.2.4 LCO/NRES

We conducted high resolution spectroscopy of HD 18599 using Las Cumbres Observatory's (*LCO* ; Brown et al. 2013) Network of Robotic Echelle Spectrographs (*NRES* ; Siverd et al. 2018). It has a spectral resolution of 53 000 with wavelength coverage between 3800 and 8600 Å. The observations were conducted on several nights with exposure times between 480 s and 1200 s, resulting in one observation at the unit at the Cerro-Tololo Inter-American Observatory (CTIO) in Chile and two observations at the South African Astronomical Observatory (SAAO). All three observations consisted of three consecutive exposures which were binned on a nightly basis. Due to weather conditions, only two out of the three nightly binned spectra had enough SNR for a confident spectral classification using the SPECMATCH-SYNTH code.[5] The spectrum obtained at the *LCO* CTIO node has SNR = 102 and the spectrum obtained at the *LCO* SAAO node has SNR = 45. We note that the stellar parameters from the spectral classification are in agreement with the ones from the isochrone estimates.

2.3 *Gaia* astrometry

Between 25 July 2014 and 23 May 2016, the ESA *Gaia* satellite measured about 300 billion centroid positions of 1.6 billion stars. The positions, proper motions, and parallaxes of the brightest 1.3 billion sources were calculated for the second data release (DR2) (Gaia Collaboration 2018). HD 18599 was assigned the *Gaia* DR2 identifier 4728513943538448512 , and had 265 'good' astrometric

---

[4]https://c-munipack.sourceforge.net

[5]https://github.com/petigura/specmatch-syn

Table 2. Summary of our follow up photometric observations.

Telescope	Camera	Filter	Pixel scale (arcsec)	Estimated PSF (arcsec)	Photometric Aperture Radius (pixel)	Transit Coverage	Date (UT)
LCO-CTIO (1.0 m)	Sinistro	B	0.39	1.73	12	full	2021-09-18
LCO-CTIO (1.0 m)	Sinistro	z_s	0.39	1.49	12	full	2021-09-18
MKO CDK700 (0.7 m)	U16	i'	0.401	5.0	21	full	2020-11-28
NGTS (0.2 m)	iKon-L 936	NGTS	4.97	3.5	8.5	full	2019-11-21
Spitzer (0.8 m)	IRAC	IRAC2: 4.5 (1.0) μm	1.2	1.1	–	full	2019-04-29
PEST (0.3 m)	ST-8XME	Ic	1.23	5.3	7	full	2019-01-07
LCO-CTIO (0.4 m)	SBIG 0.4m	i'	0.571	3.45	14	partial	2018-12-22
LCO-CTIO (1 m)	Sinistro	u'	0.389	2.66	10	full	2018-11-23
LCO-CPT (1 m)	Sinistro	g'	0.389	–	30	full	2018-11-18
IRSF (1.4 m)	SIRIUS	J, H, K	0.453	–	10	full	2018-10-16

Table 3. HD 18599 radial velocities.

Time [BJD-2450000)]	RV (m s^{-1})	σ_{RV} (m s^{-1})	Instrument
8490.0712	−9.4571	4.3344	MINERVA-Australis
8490.0926	−0.6974	4.1199	MINERVA-Australis
8494.0647	21.0941	4.2761	MINERVA-Australis
⋮	⋮	⋮	⋮

Note. This table is published in its entirety in a machine-readable format. A few entries are shown for guidance regarding form and content.
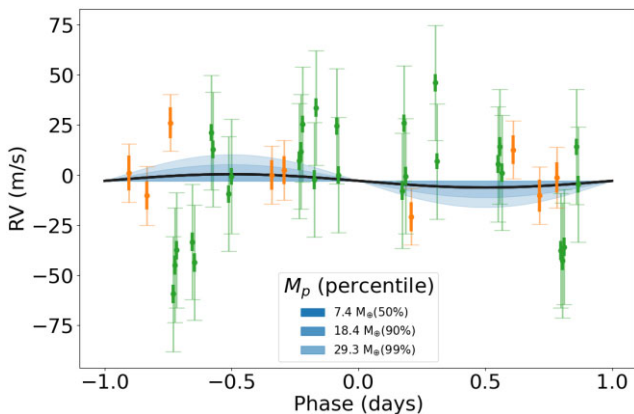
Figure 5. Phase-folded RVs with Keplerian models corresponding to the 1-, 2-, and 3-σ mass upper limits fitted to the MINERVA-Australis (green) and *FEROS* (orange) data. Error bars with dark shades show the errors estimated from our spectroscopic analyses. The error bars with lighter shades show the original errors + jitter term value (added in quadrature) from the best-fitting RV model (black line, best $M_p = 7.4 M_\oplus$).

observations, indicating a nearby ($d = 38.6$ pc), high-proper motion ($−36.68$, 50.60 mas yr^{-1}) star.

We further leverage *Gaia* DR2 to search for direct and indirect evidence of potential contaminating sources. In our sample, we can probe *Gaia* DR2 sources separated from the target as close as 1 arcsec. *Gaia* DR2 can also be useful to look for hints of binarity. Evans (2018) proposed that systems with large Astrometric Goodness of Fit of the astrometric solution for the source in the Along-Scan direction ($GOF_{AL} > 20$)) and Astrometric Excess Noise significance ($D > 5$).[6] are plausibly poorly resolved binaries. Stars

[6]For details, see: https://gea.esac.esa.int/archive/documentation/GDR2/Gaia _archive/chap_datamodel/sec_dm_main_tables/ssec_dm_gaia_source.html
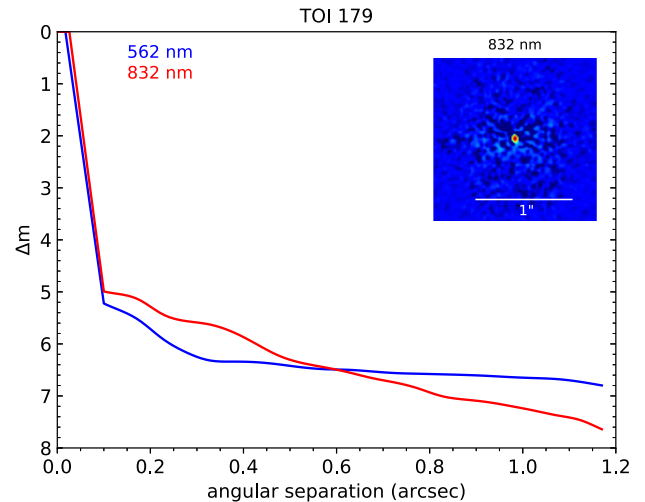

Figure 6. The contrast curves in 562 and 832 nm taken by Gemini/Zorro speckle taken by the Gemini-South telescope. The inset is a reconstructed speckle image.

that are exceptionally bright or have high proper motion are proposed to explain the large offset due causing difficulties in modelling saturated or fast-moving stars, rather than unresolved binarity. We found $GOF_{AL} = 7.0$ and $D = 0$ for HD 18599 which are well below the aforementioned empirically motivated cutoffs, indicating the target is indeed single.

2.4 Gemini speckle imaging

The presence of multiple unresolved stars in photometric and spectroscopic observations of a transiting planetary system biases measurements of the planet's radius, mass, and atmospheric conditions (e.g. Southworth & Evans 2016; Furlan & Howell 2020). To determine if any fainter point sources existed closer to target inside of *Gaia*'s point-source detection limits and to rule out false positives caused by an eclipsing binary as well as to search for potential (sub-)stellar companions within a few arcseconds from the target, we conducted speckle imaging using the Zorro instrument in *b* and *r* cameras centered on 562 and 832 nm, respectively, mounted on the 8.1 m Gemini South Telescope at the Cerro Pachon, Chile (Scott et al. 2021). Smooth contrast curves were produced from the reconstructed images by fitting a cubic spline to the 5-σ sensitivity limits within a series of concentric annuli. The speckle observations with their corresponding contrast curves in Fig. 5 illustrate that no companions

were detected within a radius of 1.2 arcsec down to a contrast level of 7 magnitudes, and no close companion star was detected within angular resolutions of the diffraction limit (0.02 arcsec) out to 1.2 arcsec. At the distance of HD 18599 ($d = 38.6$ pc), these limits correspond to spatial limits of 0.8 to 46 AU. These observations sharply reduce the possibility that an unresolved background star is the source of the transits. The contrast curves are also used as additional constraints for false positive calculation in Section 4.4.

3 HOST STAR PROPERTIES

HD 18599 (HIP 13754, TOI 179, TIC 207141131) is a known young, nearby K2V star included in the SPHERE GTO The SpHere INfrared survey for Exoplanets (SHINE) survey sample (Chauvin et al. 2017). Based on 16 HARPS spectroscopic observations, Grandjean et al. (2020, 2021) did not detect any planetary companion. They also measured a systemic RV $= 115.9 \pm 38.9$ m s^{-1} (rms) and chromospheric flux ratio of $\log R'_{HK} = -4.310$ indicating a high activity index mainly due to stellar starspots. In the following, we characterize the host star in detail.

3.1 Fundamental parameters

3.1.1 *isochrones*

To obtain the physical properties of HD 18599, we utilized the Python package `isochrones` (Morton 2015a)[7] that relies on the MESA Isochrones & Stellar Tracks (MIST; Dotter 2016) grid to infer stellar parameters using a nested sampling scheme given photometric or spectroscopic data and other empirical constraints. In particular, we used 2MASS (*JHKs*) (Skrutskie et al. 2006) and along with *Gaia* DR2 parallax (Gaia Collaboration 2018) and extinction. We corrected the parallax for the offset found in Stassun & Torres (2018) while quadratically adding 0.1 mas to the uncertainty to account for systematics in the *Gaia* DR2 data (Luri et al. 2018). Additionally, we used $T_{\rm eff}$, $\log g$, and [Fe/H] derived from spectroscopy (see Section 2.2) or taken from the literature as additional priors. The results of `isochrones` are summarized in Table 4.

3.1.2 *Spectral energy distribution*

This section presents an independent method to derive empirical stellar parameters of HD 18599 which also serves to cross-check our results obtained from the `isochrones` method (Section 3.1.1). Following the procedures described in Stassun & Torres (2016); Stassun, Collins & Gaudi (2017); Stassun et al. (2018), we first construct the broad-band spectral energy distribution (SED) of HD 18599, and then derive the stellar radius using the *Gaia* DR2 parallax. The broad-band photometry measurements include the FUV and NUV magnitudes from *GALEX*, the $B_T V_T$ magnitudes from *Tycho-2*, the *JHK_S* magnitudes from *2MASS*, the W1–W4 magnitudes from *WISE*, and the $GG_{\rm RP}G_{\rm BP}$ magnitudes from *Gaia*. Altogether, the available photometry spans the full stellar SED over the wavelength range 0.2–22 μm. Then, we fit the SED with the NextGen stellar atmosphere models taking into account the effective temperature ($T_{\rm eff}$) and metallicity ([Fe/H]) derived from the spectroscopic analysis. The extinction (A_V) was set to zero because of the star being very near at d = 40 pc.

[7] http://github.com/timothydmorton/isochrones; v.2.1

Table 4. Stellar parameters for HD 18599.

Parameter	Value	Provenance
Catalogue information		
R.A. (hh:mm:ss)	02:57:02.88	*Gaia* DR2
Decl. (dd:mm:ss)	-56:11:30.73	*Gaia* DR2
μ_α (mas yr^{-1})	-36.68 ± 0.04	*Gaia* DR2
μ_δ (mas yr^{-1})	50.60 ± 0.05	*Gaia* DR2
Parallax (mas)	25.90 ± 0.11†	*Gaia* DR2
RV (km s^{-1})	-0.484 ± 0.261	*Gaia* DR2
Distance (pc)	38.57 ± 0.04	Bailer-Jones et al. (2018)
TOI ID	179	–
TIC ID	207 141 131	–
HIP ID	13 754	–
HD ID	18 599	–
Gaia DR2 ID		
	4 728 513 943 538 448 512	
Broad-band magnitudes		
G	8.73 ± 0.01	*Gaia* DR2
B$_P$	9.21 ± 0.01	*Gaia* DR2
R$_P$	8.14 ± 0.01	*Gaia* DR2
J	7.428 ± 0.018	2MASS
H	7.029 ± 0.015	2MASS
K	6.883 ± 0.02	2MASS
TESS	8.18 ± 0.01	TIC v8
Stellar properties from CHIRON spectra		
$T_{\rm eff}$ (K)	$5220 \pm 50K$	This work
$\log g$ (dex)	4.6 ± 0.1	This work
[Fe/H] (dex)	-0.1 ± 0.1	This work
Li I EW (mÅ)	41 ± 7	This work
Stellar properties from NRES spectra		
$T_{\rm eff}$ (K)	5155 ± 100	This work
$\log g$ (dex)	4.60 ± 0.10	This work
[Fe/H] (dex)	0.13 ± 0.06	This work
$v \sin i$ (km s^{-1})	3.52 ± 0.88	This work
Stellar properties from FEROS spectra		
Li I EW (mÅ)	42 ± 2	This work
Stellar properties from SED		
$R_\star$ ($R_\odot$)	0.781 ± 0.016	This work
$F_{\rm bol}$ (erg s^{-1} cm^{-2})	$8.013 \pm 0.093 \times 10^{-9}$	This work
$L_{\rm bol}$ ($L_\odot$)	0.3709 ± 0.0044	This work
Stellar properties from isochrones (adopted)		
$R_\star$ ($R_\odot$)	0.78 ± 0.01	This work
$M_\star$ ($M_\odot$)	0.84 ± 0.03	This work
$T_{\rm eff}$ (K)	5241 ± 44	This work
$\log g$ (dex)	4.58 ± 0.02	This work
[Fe/H] (dex)	-0.08 ± 0.07	This work
A_V (mag)	0.21 ± 0.14	This work
$V \sin i$ (km s^{-1})	3–9	This work
$P_{\rm rot}$ (d)	8.7	This work
age (Myr)	300 ± 120	This work

Note. †0.1 mas was added in quadrature.

Fig. 6 shows the SED plot with broad-band photometry measurements superposed with the best-fitting model. The resulting fit is excellent with a reduced χ^2 of 1.9 (excluding the *GALEX* FUV and NUV fluxes, which are consistent with moderate chromospheric activity). Integrating the unreddened SED model yields the bolometric flux at Earth of $F_{\rm bol} = 8.013 \pm 0.093 \times 10^{-9}$ erg s^{-1} cm^{-2}. Taking the $F_{\rm bol}$ and $T_{\rm eff}$ together with the *Gaia* DR2 parallax, which was adjusted to account for the systematic offset reported by Stassun & Torres (2018), yields the stellar radius as $R_\star = 0.781 \pm 0.016$ R$_\odot$. In addition, the stellar bolometric luminosity is obtained directly from $F_{\rm bol}$ and the parallax yields $L_{\rm bol} = 0.3709 \pm 0.0044$ L$_\odot$. Finally, we
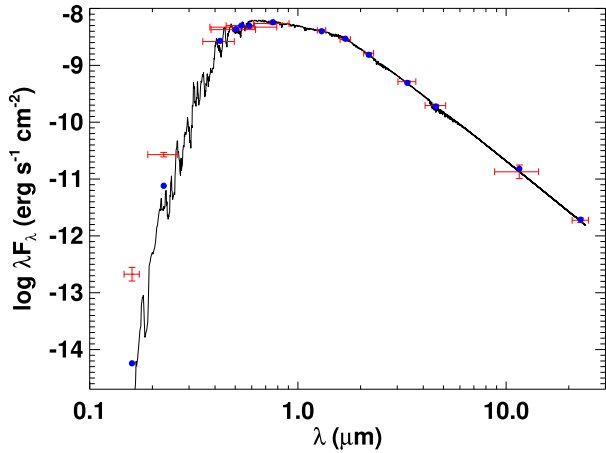
Figure 7. Spectral energy distribution (SED) of HD 18599 . The red symbols represent the observed photometric measurements, where the horizontal bars represent the effective width of the passband. The blue symbols are the model fluxes from the best-fitting NextGen atmosphere model (black).
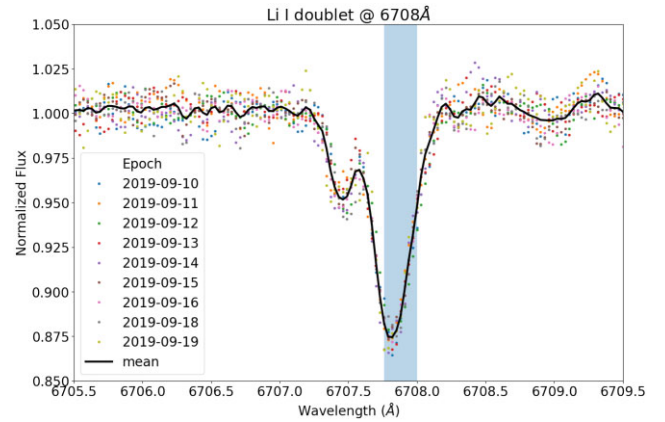

Figure 8. *FEROS* spectra zoomed around the Li I doublet absorption at 6708 Å (shaded blue region) which is a known strong indicator of youth. The black line is the mean of all spectra taken at different epochs.

estimate the stellar mass from the empirical relations of Torres (2010) and a 6 per cent error from the empirical relation itself yields $M_\star = 0.87 \pm 0.05\ M_\odot$, whereas the mass estimated empirically from $R_\star$ together with the spectroscopic $\log g$ yields $M = 0.56 \pm 0.13\ \mathrm{M_\odot}$. This discrepancy suggests that the spectroscopic $\log g$ may be slightly underestimated. In any case, these values are in agreement with the values estimated using `isochrones` method in Section 3.1.1 which uses high-resolution spectra. The final values are listed in Table 4.

3.2 Youth indicators

Soderblom et al. (2014) provides a comprehensive review of the techniques to determine approximate stellar ages. To age-date HD 18599 , first we search for coeval, phase-space neighbours and compile a sample of candidate siblings to compare with the empirical sequences of young clusters (colour–magnitude diagram, R'_{HK}, Li I λ6708 equivalent width, stellar rotation period) and gyrochonology relationships. Age dating stars is notoriously difficult except for an ensemble of stars. Hence, most of the currently known young stars hosting transiting planets are found in stellar associations where age can be reliably measured. In fact, the youngest transiting host star known so far, K2-33, is found in a 5–10 Myr moving group in Upper Sco. According to MESA grids, the Pre-Main Sequence (PMS) contraction time of a $M_\star = 0.8 \mathrm{M_\odot}$ star is ∼67 Myr. Thus, the parameters of the star do not significantly change between 0.1 and 1 Gyr.

Grandjean et al. (2021) measured the age of HD 18599 to be 200^{+200}_{-75} Myr based on lithium depletion. Moreover, Stanford-Moore et al. (2020) estimated the age of HD 18599 to be 681 Myr (or 293–2210 Myr at 68 per cent confidence level) using the BAFFLES[8] code that utilizes the calcium emission strength ($\log R'_{HK}$) and/or lithium abundance (Li EW) and B–V colour. In the following, we use new spectrum to measure the lithium equivalent width and also use recent data to measure the rotation period to derive a more precise age of HD 18599 .

3.2.1 Stellar association

HD 18599 is previously known to be a young field star based on previous studies (Grandjean et al. 2020, 2021). Thus, it comes to no surprise that we did not find HD 18599 to be a member of any of the 1641 clusters catalogued in Cantat-Gaudin & Anders (2020) as well as among the young moving groups identified in Gagné et al. (2018) and Gagné & Faherty (2018). We double checked for co-moving stars in the neighbourhood by querying the kinematics of all sources within 10 arcmin of the target from the *Gaia* DR2 catalogue and found no match as found using the `comove`[9] code. We found a match in TGv8 catalogue (Carrillo et al. 2020) using 4728513943538448512 and found the probability of HD 18599 being in the Galactic thin and thick disc to be 98.5 per cent and 1.4 per cent, respectively. This is not surprising given HD 18599 's high galactic latitude of ∼53 deg.

3.2.2 Li I 6708 Å equivalent width

The strength of the lithium 6708 Å absorption feature has traditionally been used as a youth indicator for Sun-like stars (Soderblom et al. 2014). When mixed down into a layer in a star that is roughly 2.5×10^6 K, Li is burned into heavier elements, and thus rapidly destroyed within the first ∼500 Myr. Thus, measuring the lithium 6708 Å absorption feature is strong evidence that the star's age is less than 1 Gyr. We inspected Li I λ6708 in *FEROS* and *CHIRON* spectra to confirm the youth of HD 18599 . As shown in Fig. 7, we measured an equivalent width (EW) of 42 ± 2 mÅ where the uncertainty comes from the standard deviation of EW measurement for each spectra. As shown in Fig. 8, we compare the Li absorption feature of HD 18599 against stars in the younger (0.1 Gyr) Pleiades cluster and the much older (>1 Gyr) *Kepler* stars, as a function of effective temperature. Clearly, the Li I λ6708 equivalent widths of HD 18599 is intermediate between the *Kepler* stars and Pleiades stars, consistent with our age estimate for HD 18599 . Although not shown in the figure for clarity, this Li strength generally agrees with those found in stars in Hyades and Praesepe corresponding to an age of 800 Myr. The EW width is also narrower than those measured by Bowler et al. (2019) for 58 Li-rich K to M stars (100–600 mÅ) in the solar neighbourhood with ages between 10 and 120 Myr.
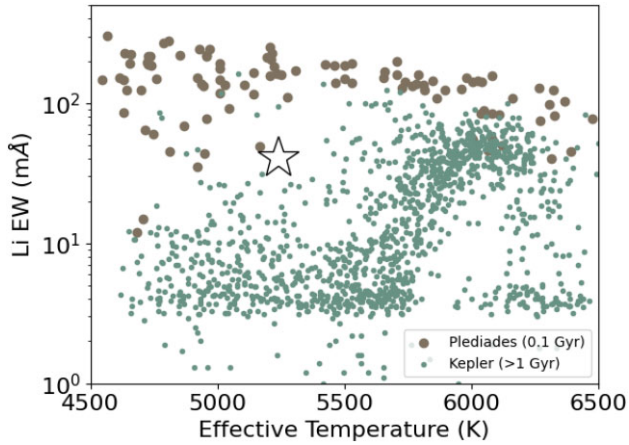
[8]https://github.com/adamstanfordmoore/BAFFLES

[9]https://github.com/adamkraus/Comove

Figure 9. T_{eff} versus equivalent width of HD 18599 (masked as star) compared to Pleiades (age 0.1 Gyr) and *Kepler* field stars (>1 Gyr).

3.2.3 Activity indicators

We can also estimate the stellar age by taking advantage of the observed chromospheric activity together with empirical age–activity-rotation relations. For example, taking the chromospheric activity indicator, $\log R'_{HK} = -4.41 \pm 0.02$ from Boro Saikia et al. (2018) and applying the empirical relations of Mamajek & Hillenbrand (2008), gives a predicted age of 0.30 ± 0.05 Gyr. Whilst this star is an X-ray source based on detection from *ROSAT*, the X-ray strength is weak ($\log Lx/Lbol = -4.64 \pm 0.25$) which corresponds to $1 - \sigma$ age range from X-ray of 475^{+734}_{-305} Myr. The X-ray count to luminosity calibration is from Fleming, Schmitt & Giampapa (1995), and the X-ray luminosity to age calibration is from equation (A3) in Mamajek & Hillenbrand (2008).

3.2.4 Stellar rotation period and amplitude

The top panel in Fig. 2 clearly shows significant spot-modulated rotational signals in the *TESS* light curves. To measure the rotation period of HD 18599, we used the light curves from *TESS* PDCSAP and *KELT* (Oelkers et al. 2018). The top panel in Fig. 9 shows the Lomb–Scargle (LS) periodogram of the four sectors of *TESS* (red) and the 6-yr *KELT* light curves (black). Both show a consistent peak at $P_{\mathrm{rot}} = 8.8$ d. The bottom panel in Fig. 9 shows the spot evolution of HD 18599 over each of four *TESS* sectors. We note that the light curves from sectors 2 and 3 showed a strong secondary peak at 1/2 rotation period in the LS periodogram, with the corresponding phase folded light curve showing that the star likely has large spot regions on both hemispheres. By sectors 29 and 30, these spots had evolved such that the 8.71-d period is the dominant frequency in the periodogram, which we also confirmed from *KELT* light curves. We also note that the stellar rotation period does not coincide with the planetary orbital period.

We can further corroborate the activity-based age estimate by also using empirical relations to predict the stellar rotation period from the activity. For example, the empirical relation between R'_{HK} and rotation period from Mamajek & Hillenbrand (2008) predicts a rotation period for this star of 9.7 ± 1.3 d, which is compatible with the rotation periods above as well as with the P_{rot} of 8.69 d reported by *KELT*, and also compatible with the projected rotation period inferred from the spectroscopic $v\sin i$ and $R_\star$ which gives $P_{\mathrm{rot}}/\sin i = 7.2 \pm 3.3$ d. Using $P_{\mathrm{rot}} = 8.69$ d, $R_\star = 0.77\,R_\odot$, $v\sin i = 4.3\,\mathrm{km\,s^{-1}}$, we derive an inclination of 74 deg.
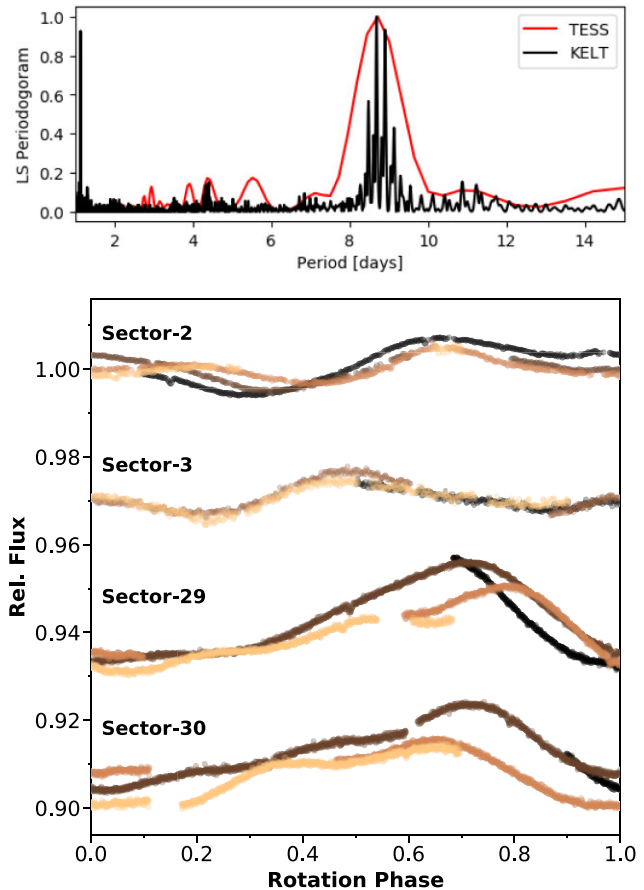
Figure 10. Rotation period estimate. The top panel shows the Lomb–Scargle periodogram of the *TESS* light curves (red) and *KELT* observations (black). The rotation period is consistently detected in both *TESS* and the six years of monitoring from *KELT*. The bottom panel shows the *TESS* light curves folded to the rotation period. Each rotation period is overplotted with a slightly different colour gradient, where the darker colour represents more recent observations.

Using the generalized Lomb–Scargle (GLS) periodogram (Zechmeister & Kürster 2009) on *TESS* light curves, we derived P_{rot} and amplitude of 8.582549 ± 0.003679 d and 0.8673 ± 0.0014 per cent, respectively. Using the age model as a function of 'smoothed' rotation amplitude presented in Morris (2020), we derived a poorly constrained age of 1145^{+1718}_{-960} Myr.

Similar to Fig. 8, we can gain more insight by qualitatively comparing the rotation period of HD 18599 with those derived from stars found in well-characterized clusters with varying ages. As shown in Fig. 10, the rotation period as a function of (decreasing) effective temperature of HD 18599 (marked with white star) locates between the younger Pleiades and Psc-Eri (0.1 Gyr) clusters and older Praesepe (0.6–0.8 Gyr), and NGC 6811 (1 Gyr) clusters. The rotation period measurements were taken from Curtis et al. (2019) and references therein.

3.2.5 Gyrochronology and adopted age

Finally, we can also estimate the age from the observed P_{rot} and empirical gyrochronology relations Mamajek & Hillenbrand (2008), we derive a median age of 386 Myr, with 3σ range of 261–589 Myr. Using Barnes (2007), we derive a median age of 247 Myr, with a 3σ range of 185–329 Myr. Fig. 11 shows the summary of the age
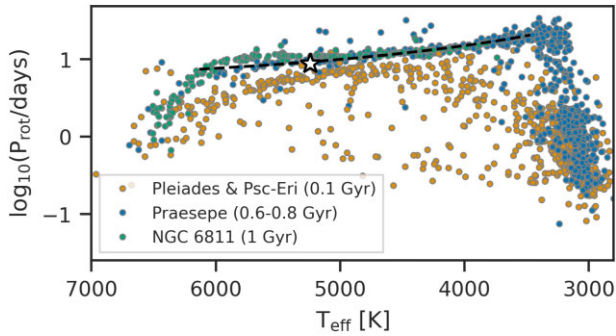
Figure 11. T_{eff} versus rotation period relation of HD 18599 (white star) compared to representative star cluster members with known ages. The black dashed line shows the negative empirical relation between rotation period and T_{eff}.
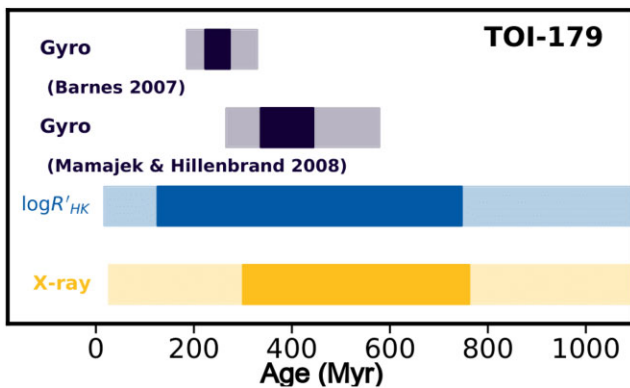

Figure 12. Summary of age estimates for HD 18599 using various methods.

estimates using the different methods consistent with the age between 0.1 and 1 Gyr. We combined the various age indicators by taking a weighted average, and we enlarged the formal uncertainty to reflect the systematic uncertainties in the different methods to arrive at an age for TOI 179 of 300 ± 120 Myr. We adopt a median age of 300 Myr for the discussion in Section 5.

4 PLANET PROPERTIES

4.1 Periodic signal search

We performed independent periodic signal search on *TESS* light curves produced from different pipelines (e.g. PDCSAP) using tql [10]. tql uses transit-least-squares [11] (Hippke & Heller 2019) for transit search and generalized Lomb–Scargle for measuring stellar rotation signal. We applied a bi-weight filter using wotan [12] with a window length of 0.5 d to detrend the stellar variability in the concatenated light curves in sectors 2 & 3, separately from sectors 29 & 30 due to the long gap. A transit signal with 4.13 d with a signal detection efficiency (SDE; Pope, Parviainen & Aigrain 2016) of 17 and a 1.75 h duration was detected. No other significant periodic transit signal was detected in further iterations.

4.2 Transit modelling

In Section 2.1.2, we confirmed that the *TESS* signal indeed originates from HD 18599. In the following, we model the *TESS* and *Spitzer* light curves jointly to robustly measure the planet's parameters, in particular the transit depth as a function of bandpass.

After removing all flagged cadences and those that are more than 3-σ above the running mean, we flattened and normalized the raw light curves using a median filter with kernel size of 301 cadences corresponding to $\sim$5 × the transit duration. After the pre-processing steps, we model the *TESS* and *Spitzer* light curves using the Python package allesfitter [13] detailed in Günther & Daylan (2020). In brief, allesfitter is a tool developed for joint modelling of photometric and RV data with flexible systematics models and was extensively used in related exoplanet studies with *TESS* (e.g. Huang et al. 2018; Dragomir et al. 2019). Parameter estimation is done with nested sampling using dynesty (Speagle 2020) of transit and RV models defined in ellc (Maxted 2016) and Gaussian Processes for systematics models using celerite (Foreman-Mackey et al. 2017). Our motivation to use allesfitter is its flexible capability to model the transit and RV data either separately or jointly including routines for model comparison and model convergence tests. Nested sampling is also more efficient than MCMC especially for complex models that require more than 10 model parameters.

We set the following as free parameters: the orbital period P_{orb}, mid-transit time T_0, scaled semimajor axis a/R_s, (cosine of) inclination i, and quadratic limb darkening coefficients in q-space (q_1 and q_2) as prescribed by Kipping (2013). We also fit for the logarithm of the Gaussian flux errors ($\log \sigma$), and the logarithm of the two hyperparameters of the Gaussian process (GP) model with an approximated Matérn-3/2 kernel for the out-of-transit baseline:

$$K(t) = \sigma^2(1 + 1/\epsilon) \exp^{1-(1-\epsilon)\sqrt{3}t/\rho} \times \qquad (1)$$
$$(1 - 1/\epsilon) \exp^{1-(1+\epsilon)\sqrt{3}t/\rho}, \epsilon = 0.01,$$

where σ and ρ reflect the characteristic amplitude and length scale of the GP, respectively. We also tried other kernels, such as a simple harmonic oscillator, but Matérn-3/2 kernel yielded the highest Bayesian evidence.

We ran several transit fits using *TESS*-only, *Spitzer*-only, and joint data set. The result of individual fits in different bandpasses are used for confirming achromaticity and eliminating false positives (Section 4.4.1). The result of joint transit modelling is used to derive robust planet and orbital parameters. We also fit an achromatic transit model on all follow-up light curves described in Section 2.1 to demonstrate that we could detect the signal on time and on target. We used uniform priors for all transit parameters the quadratic limb darkening coefficients q_1 and q_2 following Kipping (2013), where we used (truncated) Gaussian priors, with mean and standard deviation computed using limbdark [14], which is a tool for Monte Carlo sampling an interpolated grid of the theoretical limb darkening coefficients (in the *TESS* and *Spitzer* bandpasses) tabulated by Claret, Hauschildt & Witte (2012); Claret (2017) given T_{eff}, [Fe/H], and $\log g$ of the host stars. We confirmed that this setup is justified because it yielded similar results even if we used limb darkening coefficients with wide uniform priors albeit with longer convergence time. We ran the nested sampler in dynamic mode with 500 live points until it reached the prescribed 1 per cent tolerance criterion for convergence. Based on 24 077 posterior samples, we report the

---

[10] https://github.com/jpdeleon/tql
[11] https://github.com/hippke/tls
[12] https://github.com/hippke/wotan

[13] https://github.com/MNGuenther/allesfitter; v1.2.10
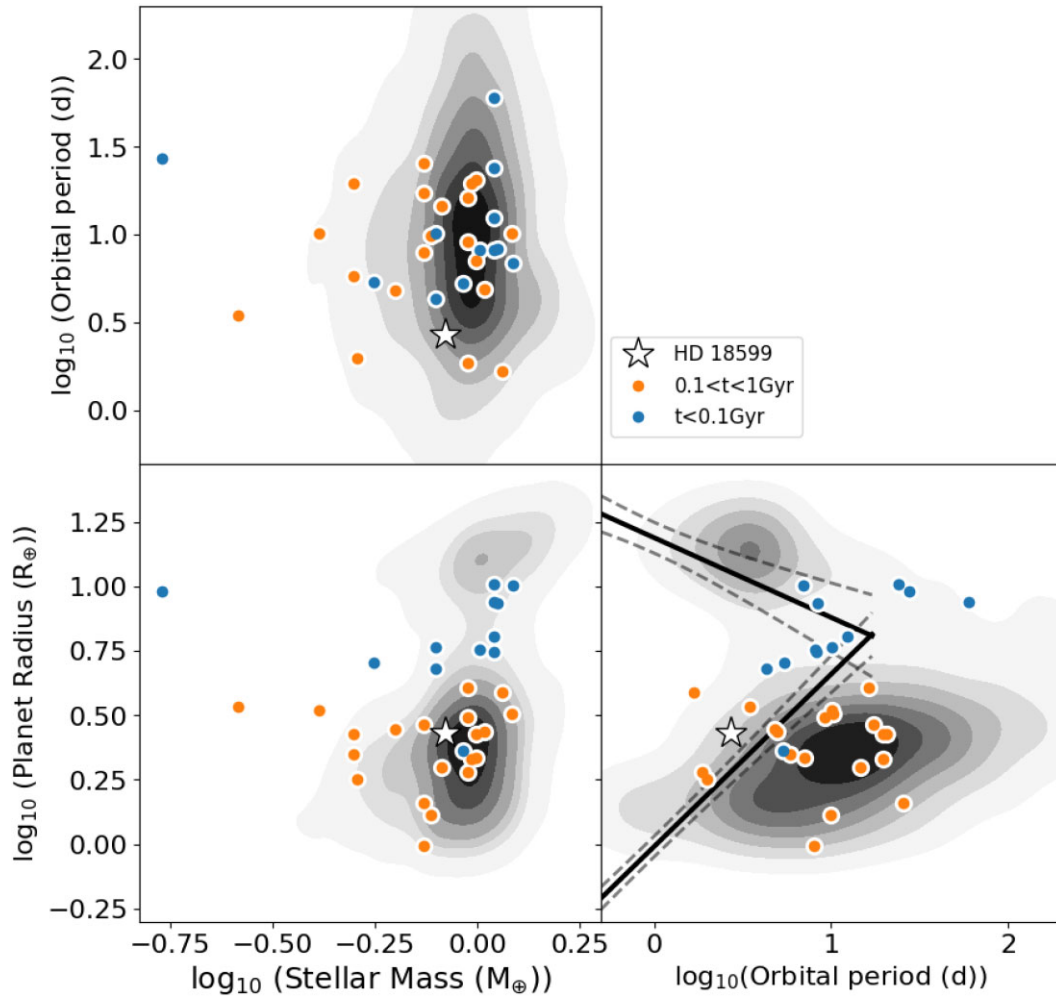[14] https://github.com/john-livingston/limbdark

Figure 14. HD 18599 (marked as star) in the context of known transiting planets orbiting older field stars (grey points). Also shown in orange and blue circles are transiting planets with age<100 Myr and 100<age<1000 Myr, respectively. The contours represent the number density of the known transiting planets orbiting older host stars. HD 18599 b appears to close to the boundaries of the Neptunian desert (solid black lines; Mazeh, Holczer & Faigler 2016) in the period-radius plane in the lower right-hand panel. The dashed lines refer to the boundaries' uncertainty regions.

HD 18599 .01 is an astrophysical false positive is small enough to formally validate it as a planet.

4.4.1 Eliminating false positive scenarios

A number of astrophysical scenarios can mimic the transit signal detected from *TESS* photometry, including eclipsing binary (EB) with a grazing geometry, hierarchical EB (HEB), and background/foreground EB (BEB) along the line of sight of the target. First, the scenario that HD 18599 is actually a grazing EB is ruled out based on the small (<1 km s^{-1}) RV variations which disfavours stellar mass companions (Section 2.2). The *TESS* light curves also do not exhibit secondary eclipses and odd–even transit depth variations. The light curve is also flat-bottomed as compared to *V*-shaped for EBs. Secondly, the scenario that HD 18599 is actually an NEB is ruled out due to the lack of *Gaia* sources found within the *TESS* and *Spitzer* photometric apertures that are bright enough to reproduce the *TESS* detection. Thirdly, the scenario that HD 18599 is actually an HEB with component stars of different colours is ruled out based on the achromatic transits from *TESS* and *Spitzer* (Section 4.2).

The most plausible HEB scenarios for HD 18599 involve pairs of eclipsing M dwarfs. Eclipses of such stars are deeper than the K-dwarf HD 18599 in longer wavelengths. Limits on whether the transit depth decreases in shorter wavelengths can therefore rule out certain HEB scenarios. Similar to the procedure described in Bouma et al. (2020), we fitted the observed depths in different bandpasses. To perform the calculation, we assumed that each system was composed of the primary star (HD 18599 , Star 1), plus a tertiary companion (Star 3) eclipsing a secondary companion (Star 2) every P_{orb} d. For a grid of secondary and tertiary star masses ranging from 0.07[17] to 0.5 M$_\odot$, we then calculated the observed maximum eclipse depth caused by Star 3 eclipsing Star 2 in *TESS* and *Spitzer* bandpasses using the following procedure. First, we interpolated $L_\star$ and T_{eff} of Star 2 and Star 3 from MIST isochrones given their masses, and the age, metallicity, and mass of Star 1 in Table 4. We then computed the blackbody functions of each stars given their T_{eff} then convolved it with the transmission functions for each band downloaded from

[17]This mass is comparable to the lowest star mass known (von Boetticher et al. 2017).

the SVO filter profile service.[18] We then integrated the result using trapezoidal method and computed the bolometric flux, F_{bol}, using the integrated functions above. Using Stefan–Boltzman law and given T_{eff} and $L_{\star}$, we computed the component radii and luminosity to derive the eclipse depth.

For an HEB system with identical component stars, these stars should be very small ($m_1 = m_2 = 0.1 M_{\odot}$) taking into account dilution from the central star to reproduce the observed *TESS* depth (∼1 ppt). In this contrived scenario, the eclipse depth in *Spitzer* I2 is about 8 times deeper than in *TESS* band, because the early M-dwarf blackbody function turns over at much redder wavelengths than the central K star blackbody (Wien's law). Thus, there is no plausible HEB configuration explored in our simulation above that can reproduce the observed depth in *Spitzer* I2. Even in the extreme case of a grazing orbit (i.e. $b = 0.99$) for the tertiary companion, the resulting decrease in eclipse depth in *Spitzer* I2 is still twice as large as the observed depth. Altogether, the multiwavelength depth constraint rules out the HEB scenario. Note that the 'boxy' shape of the transit signal especially in *Spitzer* I2 can also help rule out most of the parameter space of the HEB configurations considered above which generally produce V-shaped eclipses.

Finally, the scenario that HD 18599 is actually a BEB is negligibly small and can be completely ruled out. To quantify the probability of chance alignment of a BEB to HD 18599, we use the population synthesis code TRILEGAL[19] (Girardi et al. 2005), which simulates stellar parameters in any Galactic field. We found there is a 25 per cent chance to find an EB brighter than $T_{mag} = 15$, within an area equal to the *TESS* photometric aperture (24 *TESS* pixels ≈ 2.94 arcmin²). We can eliminate the presence of any stellar companion with $\Delta M < 5$ up exterior to 0.1 arcmin using our high spatial resolution speckle images (Section 2.4).[20] This result is consistent with the observed paucity of close binaries in *TESS* host stars (Lester et al. 2021; Ziegler et al. 2021). Within this area, we found that there is a 7.66×10^{-5} chance to find a chance-aligned star. Note that this is a conservative upper limit because this result assumes all stars are binary and preferentially oriented edge-on to produce eclipses consistent with *TESS* detection.

Although our spectroscopic analysis disfavours the existence of an BEB spectroscopically blended with HD 18599, we cannot rule out all false positive scenarios involving HEB with identical colour components. For this reason, we use VESPA to model the relevant EB populations statistically.

4.4.2 *Statistical validation with* VESPA *and* TRICERATOPS

We quantify the false positive probability (FPP) of HD 18599.01 using the Python package VESPA[21] which was developed as a tool for robust statistical validation of planet candidates identified by the *Kepler* mission (e.g. Morton 2012) and its successor *K2* (e.g. Crossfield et al. 2016; Livingston et al. 2018b; Mayo et al. 2018). In brief, VESPA compares the likelihood of planetary scenario to

the likelihoods of several astrophysical false positive scenarios involving eclipsing binaries (EBs), hierarchical triple systems (HEBs), background eclipsing binaries (BEBs), and the double-period cases of all these scenarios. The likelihoods and priors for each scenario are based on the shape of the transit signal, the star's location in the Galaxy, and single-, binary-, and triple-star model fits to the observed photometric and spectroscopic properties of the star generated using isochrones.F

As additional constraints, we used the available speckle contrast curves described in Section 2.4, the maximum aperture radius (maxrad) – interior to which the transit signal must be produced, and the maximum allowed depth of potential secondary eclipse (secthresh) estimated from the given light curves. Similar to Mayo et al. (2018), we computed secthresh by binning the phase-folded light curves by measuring the transit duration and taking thrice the value of the standard deviation of the mean in each bin. Effectively, we are asserting that we did not detect a secondary eclipse at any phase (not only at phase = 0.5) at 3-σ level. Given these inputs, we computed a formal FPP = 1.48e-11 which robustly qualifies HD 18599.01 as a statistically validated planet.

Additionally, we validated HD 18599.01 using the Python package TRICERATOPS[22] which is a tool developed to validate TOIs (Giacalone & Dressing 2020; Giacalone et al. 2021). TRICERATOPS validates TOIs by calculating the Bayesian probabilities of the observed transit originating from several scenarios involving the target star, nearby resolved stars, and hypothetical unresolved stars in the immediate vicinity of the target. These probabilities were then compared to calculate a false positive probability (FPP; the total probability of the transit originating from something other than a planet around target star) and a nearby false positive probability (NFPP; the total probability of the transit originating from a nearby resolved star). As an additional constraint in the analysis, we folded in the speckle imaging follow-up obtained with the Zorro imager on Gemini-South. For the sake of reliability, we performed the calculation 20 times for the planet candidate and found FPP = 0.0027 ± 0.0008 and NFPP = 0 (indicating that no nearby resolved stars were found to be capable of producing the observed transit). Giacalone et al. (2021) noted that TOIs with FPP < 0.015 and NFPP < 10^{-3} have a high enough probability of being bona fide planets to be considered validated. Our analysis using TRICERATOPS therefore further added evidence to the planetary nature of HD 18599.01. We now refer to the planet as HD 18599 b in the remaining sections.

5 DISCUSSION

Here, we consider the nature of HD 18599 b (= TOI 179 b) by placing it in context with the population of known exoplanets.[23] Fig. 14 shows HD 18599 (marked as star) in the context of known transiting planets orbiting >1 Gyr old field stars (black points). Also shown are transiting planets orbiting young (<100 Myr, blue) and adolescent stars (100<age<1000 Myr, orange). HD 18599 b resides in the parameter space consistent with other planets orbiting adolescent stars. In particular, HD 18599 b is most similar to K2-284 b in terms of orbital period and radius among the known young transiting planets. K2-284 b also orbits a K-type field star with an age of 100–760 Myr, consistent with HD 18599 (David et al. 2018).

[18] http://svo2.cab.inta-csic.es/theory/fps/

[19] http://stev.oapd.inaf.it/cgi-bin/trilegal

[20] Interior to 0.1' however, we could not clearly show that there is no bright enough star in the target's current position based on the earliest archival image taken during *POSS-1* sky survey ∼60 yr ago when the target would have moved 0.94 arcmin relative to the background stars. The brightness of the target essentially masked the view along the line of sight to the target in the archival image

[21] https://github.com/timothydmorton/VESPA

[22] https://github.com/stevengiacalone/triceratops

[23] Based on a query of the NASA Exoplanet Archive 'Confirmed Planets' table on 2023 January 31, https://exoplanetarchive.ipac.caltech.edu/

When compared to transiting planets around older field stars, HD 18599 b appears to fall in the large-radius tail of the size distribution for close-in sub-Neptunes.

The measured period of P_{orb} = 4.13 d and radius of R_P = 2.7 $R_\oplus$ places it close to the boundaries of the Neptunian desert defined by Mazeh et al. (2016) as shown in the lower right-hand panel of Fig. 14. HD 18599 b joins the sparsely populated region within or near the boundaries of the Neptune desert, with the youngest among planet groups occupying the majority of such a special region. Among the known young planets, K2-100 b is located the deepest within the Neptune desert with P_{orb} = 1.67 d and R_P = 3.88 $R_\oplus$. This is unsurprising because the planet's atmosphere is still currently experiencing photoevaporative escape (Gaidos et al. 2020). The youngest in the group is K2-33 b at 5–10 Myr with P_{orb} = 5.42 d and R_P = 5.04 $R_\oplus$. In the two lower panels in Fig. 14, it is clear that the young planet population appears inflated relative to the older planet populations, especially in the case of planets orbiting low-mass stars (e.g. Mann et al. 2016; David et al. 2019; Newton et al. 2019; Bouma et al. 2020; Rizzuto et al. 2020). However, most transiting planets found orbiting adolescent stars like HD 18599 do not appear to be clear outliers in the period–radius diagram (e.g. David et al. 2018; Livingston et al. 2018a; Mann et al. 2020). One possible explanation for this observed behaviour comes from photoevaporation theory. Young stars emit X-ray and EUV radiation strong enough to drive atmospheric escape. In this picture, atmospheric loss operates in a time-scale on the order of hundreds of millions of years for close-in planets with thick atmospheres to a few billion years for the largest and most massive planetary cores (David et al. 2020).

Another explanation for the anomalously large radii of young planets comes from core-powered mass-loss theory (Gupta & Schlichting 2019). In this picture, the cooling of the planetary core provides the energy for atmospheric loss. This effect alone effectively reproduces the observed valley in the radius distribution of small close-in planets (Fulton et al. 2017). More recently, Berger et al. (2020) found the first evidence of a stellar age dependence of the planet populations straddling the radius valley. They found that the fraction of super-Earths to sub-Neptunes increases from 0.61 ± 0.09 at young ages (<1 Gyr) to 1.00 ± 0.10 at old ages (>1 Gyr), consistent with the prediction by core-powered mass-loss which operates on a gigayear time-scales. For a mini-Neptune with a predominantly H2-He envelope presumably similar to HD 18599 b, its radius will contract to approximately half of its original size in the first 500 Myr due to radiative cooling and XUV-driven mass-loss (Howe & Burrows 2015). Given the wide age range of HD 18599 b, it is difficult to ascertain whether enough time has passed to allow HD 18599 b to contract to its final equilibrium radius and whether either one or combination of both effects is responsible for the observed properties of HD 18599 b. At this point, we cannot be sure that the relatively large size of HD 18599 b is due to its young age. However, the properties of HD 18599 b do not appear to be merely a consequence of observational bias.

6 SUMMARY AND FUTURE PROSPECTS

Young exoplanets inhabit a very important part of the exoplanet evolutionary time-scale, where formation mechanisms, accretion, migration, and dynamical interactions can significantly change the shape of observed planetary systems. To date, only a handful of planetary systems <1 Gyr old are known. The main reason for the rarity of known young planets is the strong stellar activity of young stars, which makes it hard to find the subtle planetary signal in the face of large stellar variations (e.g. Plavchan et al. 2020).

Despite the challenges, the young planet population is an emerging field that is expected to yield highly impactful scientific results. Therefore, by compiling a statistically significant sample of well-characterized exoplanets with precisely measured ages, we should be able to begin identifying the dominant processes governing the time-evolution of exoplanet systems. In this light, we present the discovery and validation of a sub-Neptune orbiting the young star HD 18599. Complementary to *TESS* data, we utilized a suite of follow-up data including photometry with *Spitzer*/IRAC, IRSF/SIRIUS, & *KELT*, speckle imaging with Gemini/Zorro, and high resolution spectroscopy from ESO 2.2m/*FEROS*, *LCO* 2m/*NRES*, SMARTS 1.5m/*CHIRON*, & MKO 4x0.7m/. By implementing a similar validation framework and analyses presented previously, we found that the planet has an orbital period of 4.13 d, a radius of 2.7 $R_\oplus$, a mass of $<0.4 M_{JUP}$, and an equilibrium temperature of 934 ± 10 K. When compared to transiting planets around older field stars, HD 18599 b appears to fall in the large-radius tail of the size distribution for close-in sub-Neptunes.

A comparison between the typical densities of young and old planets may be more insightful than simply comparing radii and periods. However, planets around young stars are challenging for RV observations and only a handful have been successful to obtain mass measurements (e.g. Barragán et al. 2019, 2022; Zicher et al. 2022). Fortunately, the proximity and brightness of HD 18599 b would allow mass measurement with high resolution Doppler spectroscopy, unlike the majority of young *K2* planets orbiting faint host stars. Measuring the planet's mass provides a rare opportunity to derive the planet's density and model its interior composition given sufficient precision. This would then allow direct comparison of bulk parameters such as density with similar sub-Neptunes orbiting older host stars. Our estimate of mass upper limit from Section 2.2 implies an RV amplitude of at most 300 m s⁻¹. Thus, a dedicated campaign designed to observe and model the RV systematics may allow a precise mass measurement of HD 18599 b. A potential caveat is that HD 18599 is rotating faster than 15 d which results in rotational broadening at a level that limits RV precision and/or a large stellar RV jitter caused by strong stellar variability expected for young stars.

Moreover, a measurement of the planet's obliquity or the sky-projected angle between the stellar spin axis and the planet's orbital axis via observation of the Rossiter–McLaughlin (RM) effect is also a good avenue to explore. The planet's obliquity is a tracer for any dynamical processes, such as tidal interaction with stellar companions (e.g. Batygin 2012), that the system might have undergone to produce a misaligned orbit, assuming well-aligned initial condition. Obliquity measurements were conducted for a growing number of young planets (e.g. Gaidos et al. 2020; Wirth et al. 2021; Johnson et al. 2022). These planets were found to have well-aligned orbits which indicates that misalignments may be generated over time-scales of longer than tens of Myr. We estimate the RV amplitude due to the RM effect to be ≈140 m s⁻¹ using the relation $\Delta RV_{RM} = v \sin i \, (R_p/R_s)^2 \sqrt{1 - b^2}$ (Gaudi & Winn 2007), making this one of the most amenable targets for RM follow-up. This makes obliquity measurements feasible for HD 18599 b, following only DS Tau Ab and AU Mic b to have obliquity measurement among young systems so far (Martioli et al. 2020; Zhou et al. 2020). Constraining the star–planet obliquity of this young system may shed light on possible migration mechanisms (e.g. Kozai, secular, tidal interactions) to explain its current architecture such as its seemingly short period as compared to other young planets (e.g. Montet et al. 2020).

Following Kempton et al. (2018), we compute the transmission spectroscopy metric (TSM) which is a general metric useful for prioritizing of transmission spectroscopy targets for future infrared

observations e.g. with *JWST* (McElwain et al. 2020). It is defined as

$$TSM = \alpha \times \left(\frac{R_p T_{eq}}{M_p R_*^2}\right) \times 10^{-M_J/5}, \quad (3)$$

where α is a scale factor equal to 1.28 appropriate for HD 18599 b, R_p is the planet radius in Earth radii, M_p is the planet mass equivalent to $1.436 R_p^{1.7}$ appropriate for the size of HD 18599 b, R_* is the star radius in solar radii, M_J is the apparent magnitude of the host star in the J band, and T_{eq} is the planet's equilibrium temperature in K,

$$T_{eq} = 0.25^{0.25} \times T_* \sqrt{\frac{R_*}{a}}, \quad (4)$$

where a is the orbital semimajor axis in solar radii, and assuming zero albedo and full day–night heat redistribution. We computed TSM = 21 which can be interpreted as a transmission spectrum measurement with signal to noise of 21 in a 10 h window with the NIRISS instrument (Louie et al. 2018). Combined with its young age, this makes HD 18599 a compelling target for atmospheric characterization.

ACKNOWLEDGEMENTS

`tqdm` (da Costa-Luis 2019), `pandas` (The Pandas Development Team 2020), `seaborn` (Waskom et al. 2020), and `lightkurve` (Lightkurve Collaboration 2018).

DATA AVAILABILITY

The data underlying this article were accessed from MAST (https://archive.stsci.edu/hlsp/) with specific links mentioned in the article. The tables presented in this work will also be made available at the CDS (http://cdsarc.u-strasbg.fr/).

REFERENCES

Addison B. C. et al., 2021, AJ, 162, 292
Addison B. et al., 2019, PASP, 131, 115003
Andrews-Hanna J. C., Zuber M. T., Banerdt W. B., 2008, Nature, 453, 1212
Bailer-Jones C. A. L., Rybizki J., Fouesneau M., Mantelet G., Andrae R., 2018, AJ, 156, 58
Barbary K., 2016, J. Open Source Softw., 1, 58
Barber M. G. et al., 2022, AJ, 164, 88
Barnes S. A., 2007, ApJ, 669, 1167
Barragán O. et al., 2019, MNRAS, 490, 698
Barragán O. et al., 2022, MNRAS, 514, 1606
Batygin K., 2012, Nature, 491, 418
Beichman C. et al., 2016, ApJ, 822, 39
Benz W., Anic A., Horner J., Whitby J. A., 2007, Space Sci. Rev., 132, 189
Benz W., Cameron A. G. W., Melosh H. J., 1989, Icarus, 81, 113
Benz W., Slattery W. L., Cameron A. G. W., 1988, Icarus, 74, 516
Berger T. A., Huber D., Gaidos E., van Saders J. L., Weiss L. M., 2020, AJ, 160, 108
Bertin E., Arnouts S., 1996, Astron. Astrophys. Suppl. Ser., 117, 393
Boro Saikia S. et al., 2018, A&A, 616, A108
Bouma L. G. et al., 2020, AJ, 160, 239
Bouma L. G. et al., 2022a, AJ, 164, 18
Bouma L. G. et al., 2022b, AJ, 163, 121
Bowler B. P. et al., 2019, ApJ, 877, 60
Brahm R., Jordán A., Espinoza N., 2017, PASP, 129, 034002
Brown T. M. et al., 2013, PASP, 125, 1031
Bryant E. M. et al., 2020, MNRAS, 494, 5872
Cantat-Gaudin T., Anders F., 2020, A&A, 633, A99
Canup R. M., 2012, Science, 338, 1052
Canup R. M., Asphaug E., 2001, Nature, 412, 708
Carrillo A., Hawkins K., Bowler B. P., Cochran W., Vanderburg A., 2020, MNRAS, 491, 4365
Chau A., Reinhardt C., Helled R., Stadel J., 2018, ApJ, 865, 35
Chauvin G. et al., 2017, in Reylé C., Di Matteo P., Herpin F., Lagadec E., Lançon A., Meliani Z., Royer F., eds, SF2A-2017: Proceedings of the Annual meeting of the French Society of Astronomy and Astrophysics. French Society of Astronomy and Astrophysics, Paris, p. Di
Claret A., 2017, A&A, 600, A30
Claret A., Hauschildt P. H., Witte S., 2012, A&A, 546, 7
Collier Cameron A. et al., 2021, MNRAS, 505, 1699
Collins K. A., Kielkopf J. F., Stassun K. G., Hessman F. V., 2017, AJ, 153, 77
Crossfield I. J. M. et al., 2016, ApJS, 226, 7
Cumming A., Marcy G. W., Butler R. P., 1999, ApJ, 526, 890
Curtis J. L., Agüeros M. A., Mamajek E. E., Wright J. T., Cummings J. D., 2019, AJ, 158, 77
Dai F. et al., 2017, AJ, 154, 226
David T. J. et al., 2016, Nature, 534, 658
David T. J. et al., 2018, AJ, 156, 302
David T. J. et al., 2021, AJ, 161, 6
David T. J., Petigura E. A., Luger R., Foreman-Mackey D., Livingston J. H., Mamajek E. E., Hillenbrand L. A., 2019, ApJ, 885, L12
Dragomir D. et al., 2019, ApJ, 875, L7
Evans D. F., 2018, Res. Notes Am. Astron. Soc., 2, 20

Fazio G. G. et al., 1998, in Fowler A. M.ed., Proc. SPIE Conf. Ser. Vol. 3354, Infrared Astronomical Instrumentation. SPIE, Bellingham, p. 1024

Fleming T. A., Schmitt J. H. M. M., Giampapa M. S., 1995, ApJ, 450, 401

Foreman-Mackey D., Agol E., Ambikasaran S., Angus R., 2017, celerite: Scalable 1D Gaussian Processes in C++, Python, and Julia, recordascl:1709.008

Fulton B. J. et al., 2017, AJ, 154, 109

Furlan E., Howell S. B., 2020, ApJ, 898, 47

Gagné J. et al., 2018, ApJ, 856, 23

Gagné J., Faherty J. K., 2018, ApJ, 862, 138

Gaia Collaboration, 2018, A&A, 616, A1

Gaidos E. et al., 2020, MNRAS, 495, 650

Gaudi B. S., Winn J. N., 2007, ApJ, 655, 550

Giacalone S. et al., 2021, AJ, 161, 24

Giacalone S., Dressing C., 2021, Validating TESS Planet Candidates with TRICERATOPSShow affiliations

Girardi L., Groenewegen M. A. T., Hatziminaoglou E., da Costa L., 2005, A&A, 436, 895

Grandjean A. et al., 2020, A&A, 633, A44

Grandjean A. et al., 2021, A&A, 650, A39

Guerrero N. M. et al., 2021, AJS, 254, 29

Günther M. N., Daylan T., 2019, allesfitter: Flexible star and exoplanet inference from photometry and radial velocity 2019ascl.soft03003G

Gupta A., Schlichting H. E., 2019, MNRAS, 487, 24

Heitzmann A. et al., 2021, MNRAS, 505, 4

Hippke M., Heller R., 2019, A&A, 623, A39

Horner J. et al., 2020, PASP, 132, 102001

Howe A. R., Burrows A., 2015, ApJ, 808, 150

Huang C. X. et al., 2018, ApJ, 868, L39

Ingalls J. G. et al., 2016, AJ, 152, 44

Jenkins J. M. et al., 2016, in Chiozzi G., Guzman J. C.eds, Proc. SPIE Conf. Ser. Vol. 9913, Software and Cyberinfrastructure for Astronomy IV. SPIE, Bellingham, p. 99133E

Jensen E., 2013, Tapir: A web interface for transit/eclipse observability, Astrophysics Source Code Library, recordascl:1306.007

Johnson M. C. et al., 2022, AJ, 163, 247

Kaufer A., Stahl O., Tubbesing S., Nørregaard P., Avila G., Francois P., Pasquini L., Pizzella A., 1999, The Messenger, 95, 8

Kegerreis J. A. et al., 2018, ApJ, 861, 52

Kempton E. M. R. et al., 2018, PASP, 130, 114401

Kipping D. M., 2013, MNRAS, 435, 2152

Knutson H. A. et al., 2012, ApJ, 754, 22

Kuhn R. B. et al., 2016, MNRAS, 459, 4281

Lester K. V. et al., 2021, AJ, 162, 2

Liu S.-F., Hori Y., Müller S., Zheng X., Helled R., Lin D., Isella A., 2019, Nature, 572, 355

Livingston J. H. et al., 2018a, AJ, 155, 115

Livingston J. H. et al., 2018b, AJ, 156, 277

Livingston J. H. et al., 2019, AJ, 157, 102

Louie D. R., Deming D., Albert L., Bouma L. G., Bean J., Lopez-Morales M., 2018, PASP, 130, 044401

Luri X. et al., 2018, A&A, 616, A9

Lykawka P. S., Horner J., 2010, MNRAS, 405, 1375

Lykawka P. S., Horner J., Jones B. W., Mukai T., 2010, MNRAS, 404, 1272

Lykawka P. S., Horner J., Jones B. W., Mukai T., 2011, MNRAS, 412, 537

Mamajek E. E., Hillenbrand L. A., 2008, ApJ, 687, 1264

Mann A. W. et al., 2016, AJ, 152, 61

Mann A. W. et al., 2020, AJ, 160, 18

Mann A. W. et al., 2022, AJ, 163, 156

Martioli E. et al., 2020, A&A, 641, L1

Maxted P. F. L., 2016, A&A, 591, A111

Mayo A. W. et al., 2018, AJ, 155, 136

Mazeh T., Holczer T., Faigler S., 2016, A&A, 589, A75

McElwain M. W. et al., 2020, in Lystrup M., Perrin M. D., Batalha N., Siegler N., Tong E. C., eds, Proc. SPIE Conf. Ser. Vol. 11443, Space Telescopes and Instrumentation 2020: Optical, Infrared, and Millimeter Wave. SPIE, Bellingham, p. 114430T

Montet B. T. et al., 2020, AJ, 159, 112

Morris B. M., 2020, ApJ, 893, 67

Morton T. D., 2012, ApJ, 761, 6

Morton T. D., 2015a, isochrones: Stellar model grid package, recordascl:1503.010

Morton T. D., 2015b, VESPA: False positive probabilities calculator, recordascl:1503.011

Nagayama T. et al., 2003, in Iye M., Moorwood A. F. M.eds, Proc. SPIE Conf. Ser. Vol. 4841, Instrument Design and Performance for Optical/Infrared Ground-based Telescopes. SPIE, Bellingham, p. 459

Narita N., Nagayama T., Suenaga T., Fukui A., Ikoma M., Nakajima Y., Nishiyama S., Tamura M., 2013, PASJ, 65, 27

Newton E. R. et al., 2019, ApJ, 880, L17

Nicholson B. A., Hussain G., Donati J. F., Wright D., Folsom C. P., Wittenmyer R., Okumura J., Carter B. D., 2021, MNRAS, 504, 2461

Ning B., Wolfgang A., Ghosh S., 2018, ApJ, 869, 5

O'Brien D. P., Walsh K. J., Morbidelli A., Raymond S. N., Mandell A. M., 2014, Icarus, 239, 74

Oelkers R. J. et al., 2018, AJ, 155, 39

Parisi M. G., Brunini A., 1997, Planet. Space Sci., 45, 181

Pepper J., Kuhn R. B., Siverd R., James D., Stassun K., 2012, PASP, 124, 230

Pirani S., Johansen A., Bitsch B., Mustill A. J., Turrini D., 2019, A&A, 623, A169

Plavchan P. et al., 2020, Nature, 582, 497

Pope B. J. S., Parviainen H., Aigrain S., 2016, MNRAS, 461, 3399

Rizzuto A. C. et al., 2020, AJ, 160, 33

Sandoval A., Contardo G., David T. J., 2020, AJ, 911, 6

Scott N. J. et al., 2021, Front. Astron. Space Sci., 8, 138

Siverd R. J. et al., 2012, ApJ, 761, 123

Siverd R. J. et al., 2018, in Evans C. J., Simard L., Takami H.eds, Proc. SPIE Conf. Ser. Vol. 10702, Ground-based and Airborne Instrumentation for Astronomy VII. SPIE, Bellingham, p. 107026C,

Skrutskie M. F. et al., 2006, AJ, 131, 1163

Slattery W. L., Benz W., Cameron A. G. W., 1992, Icarus, 99, 167

Smith A. M. S. et al., 2020, Astron. Nachr., 341, 273

Smith J. C. et al., 2012, PASP, 124, 1000

Soderblom D. R., Hillenbrand L. A., Jeffries R. D., Mamajek E. E., Naylor T., 2014, in Beuther H., Klessen R. S., Dullemond C. P., Henning T.eds, Protostars and Planets VI. The University of Arizona Press, Tucson, p. 219

Southworth J., Evans D. F., 2016, MNRAS, 463, 37

Speagle J. S., 2020, MNRAS, 493, 3132

Stanford-Moore S. A., Nielsen E. L., De Rosa R. J., Macintosh B., Czekala I., 2020, ApJ, 898, 27

Stassun K. G., Collins K. A., Gaudi B. S., 2017, AJ, 153, 136

Stassun K. G., Corsaro E., Pepper J. A., Gaudi B. S., 2018, AJ, 155, 22

Stassun K. G., Torres G., 2016, AJ, 152, 180

Stassun K. G., Torres G., 2018, ApJ, 862, 61

Stumpe M. C. et al., 2012, PASP, 124, 985

Torres G., 2010, AJ, 140, 1158

Tsiganis K., Gomes R., Morbidelli A., Levison H. F., 2005, Nature, 435, 459

Twicken J. D. et al., 2018, PASP, 130, 064502

Vines J., et al. 2023, MNRAS, 518, 2627

von Boetticher A. et al., 2017, A&A, 604, L6

Walsh K. J., Morbidelli A., Raymond S. N., O'Brien D. P., Mandell A. M., 2012, Meteorit. Planet. Sci., 47, 1941

Wilson M. L. et al., 2019, PASP, 131, 115001

Wirth C. P. et al., 2021, ApJ, 917, L34

Wittenmyer R. A. et al., 2022, AJ, 163, 82

Wood M. L. et al., 2022, AJ, 165, 24

Zechmeister M., Kürster M., 2009, A&A, 496, 577

Zhou G. et al., 2020, ApJ, 892, L21

Ziegler C., Tokovinin A., Latiolais M., Briceno C., Law N., Mann A. W., 2021, AJ, 162, 25

[1]*Department of Astronomy, Graduate School of Science, The University of Tokyo, 7-3-1 Hongo, Bunkyo-ku, Tokyo 113-0033, Japan*

[2]*Astrobiology Center, 2-21-1 Osawa, Mitaka, Tokyo 181-8588, Japan*

^{3}*National Astronomical Observatory of Japan, 2-21-1 Osawa, Mitaka, Tokyo 181-8588, Japan*

^{4}*Department of Astronomical Science, The Graduate University for Advanced Studies, SOKENDAI, 2-21-1, Osawa, Mitaka, Tokyo 181-8588, Japan*

^{5}*Núcleo de Astronomía, Facultad de Ingeniería y Ciencias, Universidad Diego Portales, Av. Ejército 441, Santiago, Chile Centro de Astrofísica y Tecnologías Afines (CATA), Casilla 36-D, Santiago, Chile*

^{6}*Universidad de Chile, Camino el Observatorio, 1515, Las Condes, Santiago, Chile*

^{7}*University of Southern Queensland, Centre for Astrophysics, West Street, Toowoomba, QLD 4350, Australia*

^{8}*Department of Astrophysical Sciences, Princeton University, 4 Ivy Lane, Princeton, NJ 08544, USA*

^{9}*Department of Astronomy, University of Florida, 211 Bryant Space Science Center, Gainesville, FL 32611, USA*

^{10}*Department of Physics, University of Warwick, Gibbet Hill Road, Coventry CV4 7AL, UK*

^{11}*NASA Exoplanet Science Institute, California Institute of Technology, Pasadena, CA 91106, USA*

^{12}*Department of Physics and Institute for Research on Exoplanets, Universit' e de Montr' eal, Montr' eal, QC, PO Box 6128, Canada*

^{13}*Department of Physics and Kavli Institute for Astrophysics and Space Research, Massachusetts Institute of Technology, Cambridge, MA 02139, USA*

^{14}*Department of Astronomy, The University of Texas at Austin, TX 78712, USA*

^{15}*CASA, University of Colorado, Boulder, CO 80309, USA*

^{16}*Las Cumbres Observatory, Goleta, CA 93117, USA*

^{17}*Mullard Space Science Laboratory, University College London, Holmbury St Mary, Dorking, Surrey RH5 6NT, UK*

^{18}*Center for Astrophysics, Harvard and Smithsonian, 60 Garden Street, Cambridge, MA 02138, USA*

^{19}*Department of Physics and Astronomy, George Mason University, 4400 University Drive, Fairfax, VA 22030, USA*

^{20}*Department of Physics and Astronomy, University of Kansas, 1082 Malott, 1251 Wescoe Hall Dr Lawrence, KS 66045, USA*

^{21}*NASA Astrobiology Institute's Virtual Planetary Laboratory, Box 351580 Seattle, WA 98195, USA*

^{22}*Department of Astronomy, University of Maryland, College Park, MD 20742, USA*

^{23}*Department of Physics and Astronomy, University of New Mexico, 210 Yale Blvd NE, Albuquerque, NM 87106, USA*

^{24}*Department of Astronomy, University of California, Berkeley, Berkeley, CA 94720, USA*

^{25}*Komaba Institute for Science, The University of Tokyo, 3-8-1 Komaba, Meguro, Tokyo 153-8902, Japan*

^{26}*Instituto de Astrof' isica de Canarias, V' ia L' actea s/n, E-38205 La Laguna, Tenerife, Spain*

^{27}*Department of Astronomy and Tsinghua Centre for Astrophysics, Tsinghua University, Beijing 100084, China*

^{28}*Centre for Exoplanets and Habitability, University of Warwick, Gibbet Hill Road, Coventry CV4 7AL, UK*

^{29}*NASA Jet Propulsion Laboratory, Pasadena, CA 91109, USA*

^{30}*Centro de Astrobiolog' ia (CSIC-INTA), Carretera de Ajalvir km 4, Torrej' on de Ardoz, E-28850 Madrid, Spain*

^{31}*Department of Astronomy, Wesleyan University, Middletown, CT 06459, USA*

^{32}*NASA Ames Research Center, Moffett Field, CA 94035, USA*

^{33}*Intelligent Systems Division, NASA Ames Research Center, Moffett Field, CA 94035, USA*

^{34}*Department of Earth and Planetary Sciences, University of California, Riverside, CA 92521, USA*

^{35}*School of Physics and Astronomy, University of Leicester, Leicester LE1 7RH, UK*

^{36}*Department of Physics and Astronomy, University of Louisville, Louisville, KY 40292, USA*

^{37}*School of Astronomy and Space Science, Key Laboratory of Modern Astronomy and Astrophysics in Ministry of Education, Nanjing University, Nanjing 210046, Jiangsu, China*

^{38}*Observatoire de Gen' eve, Chemin Pegasi 51, CH-1290 Versoix, Switzerland*

^{39}*Instituto de Astrof' isica de Canarias, E-38205 La Laguna, Tenerife, Spain*

^{40}*Department of Multi-Disciplinary Sciences, Graduate School of Arts and Sciences, The University of Tokyo, 3-8-1 Komaba, Meguro, Tokyo 153-8902, Japan*

^{41}*Las Cumbres Observatory Global Telescope, 6740 Cortona Dr, Suite 102, Goleta, CA 93111, USA*

^{42}*Department of Physics, University of California, Santa Barbara, CA 93106-9530, USA*

^{43}*Departamento de Matem' atica y F' isica Aplicadas, Universidad Cat' olica de la Sant' iĂ, sima Concepci' on, Alonso de Rivera 2850, Concepci' on, Chile*

^{44}*NASA Goddard Space Flight Center, 8800 Greenbelt Rd, Greenbelt, MD 20771, USA*

^{45}*Department of Earth, Atmospheric and Planetary Sciences, Massachusetts Institute of Technology, Cambridge, MA 02139, USA*

^{46}*Department of Aeronautics and Astronautics, MIT, 77 Massachusetts Avenue, Cambridge, MA 02139, USA*

^{47}*Institute of Planetary Research, German Aerospace Center (DLR), Rutherfordstr. 2, D-12489 Berlin, Germany*

^{48}*Department of Physics and Astronomy, Vanderbilt University, VU Station 1807, Nashville, TN 37235, USA*

^{49}*Department of Physics, Fisk University, Nashville, TN 37208, USA*

^{50}*Perth Exoplanet Survey Telescope, Perth, Western Australia*

^{51}*Exoplanetary Science at UNSW, School of Physics, UNSW Sydney, NSW 2052, Australia*

^{52}*Shanghai Astronomical Observatory, Chinese Academy of Sciences, Shanghai 200030, China*

This paper has been typeset from a TEX/LATEX file prepared by the author.